J. Fluid Mech. (2013), *vol.* 719, *pp.* 203–229. © Cambridge University Press 2013
doi:10.1017/jfm.2012.641

Stationary plume induced by carbon dioxide dissolution

F. Nadal[1], P. Meunier[2,†], B. Pouligny[3] and E. Laurichesse[3]

[1]Commissariat à l'Énergie Atomique (CEA), 33314 Le Barp, France
[2]IRPHE UMR 7342, CNRS, Aix Marseille Université, Centrale Marseille, 13013 Marseille, France
[3]CRPP UPR 8641, CNRS, Université Bordeaux I, 33600 Pessac, France

(Received 26 July 2012; revised 15 October 2012; accepted 20 December 2012;
first published online 19 February 2013)

In this paper, laminar convection flows induced by carbon dioxide absorption are addressed from experimental, numerical and theoretical points of view. A vertical glass tube (of centimetre scale) filled with distilled water is subjected to a sudden increase in the partial pressure of carbon dioxide. As a result of the diffusion of the gas into the unsaturated solution, a thin layer of fluid located underneath the surface becomes heavier. This initial density gradient first destabilizes to form a plume, which goes downwards through the entire cell. After a first transient pulsating regime (periodic succession of such Rayleigh–Bénard plumes), a stationary flow settles in the tube, which is maintained by the constant supply of gas at the surface. At late stages, this stationary regime is followed by an aperiodic regime, which lasts until the complete saturation of the solution (thermodynamic equilibrium). The present study only focuses on the stationary regime, whose characteristics appear to be almost independent of the Bond number and the aspect ratio but strongly dependent on the chemical Rayleigh number. Three decades of Rayleigh numbers are explored using particle image velocimetry measurements, which allows for a precise determination of the scaling exponents for the vertical velocity amplitude and the plume width. The assumption that gravity and a constant pressure gradient balance the viscous effects enables us to derive an analytic expression for the stationary vertical velocity on the axis, which scales as $Ra^{2/3}\,(\ln Ra)^{1/3}$. As a consequence, the width of the plume scales as $Ra^{-1/6}\,(\ln Ra)^{-1/3}$ and the mass Nusselt number as $(Ra/\ln Ra)^{1/3}$. These scalings are in excellent agreement with the experimental and numerical results. The multiplicative constants of these scalings can also be calculated and show a fairly good agreement if a rigid boundary condition (no-slip) is assumed at the free surface.

Key words: buoyancy-driven instability, convection, plumes/thermals

1. Introduction

Despite the extensive literature on plumes created by a point source, there have been very few studies on plumes generated by an extended source. The goal of this paper is to analyse experimentally and theoretically the structure and the amplitude of a chemical plume created by a surface of finite size.

† Email address for correspondence: meunier@irphe.univ-mrs.fr

https://doi.org/10.1017/jfm.2012.641 Published online by Cambridge University Press

Since it was suggested by Morgan (1971) that plate tectonics could originate from strong thermal convection flows in the mantle, plume study has been a topic of constant interest. As proposed by Anderson (1975), these plumes could also result from chemical inhomogeneities in the deep mantle. More recently, chemical plumes have been studied in the scope of the very controversial problem of ocean carbon dioxide disposal (see e.g. Alendal, Drange & Haugan 1994; Adams *et al.* 1995; Caulfield 1996; Aya, Yamane & Shiozaki 1999). In fact, chemical buoyancy-driven convection plays a central role in a great number of geophysical, biophysical and environmental applications. We do not intend here to present an exhaustive picture of the former literature on plumes. However, different aspects of the problem, which are not strictly connected to the situation treated in the present paper, deserve to be mentioned. The case of turbulent buoyancy flows (chemical and thermal) is of great importance in environmental physics. Pioneering works on the topic were published by Batchelor (1954) and Morton, Taylor & Turner (1956), based on the now classical entrainment assumption. Review articles written by Turner (1969), List (1982) and Woods (2010) provide a first overview on the topic. Recent experimental, numerical and theoretical works have been published by Pesci, Porter & Goldstein (2003), Dombrowski *et al.* (2005), Schofield & Restrepo (2010) and Lombardi *et al.* (2011) on the behaviour of plumes in a stably stratified environment. Within the scope of geological applications, various authors (see e.g. Olson, Schubert & Anderson 1993) have taken into account the variation of viscosity with temperature, which led to narrow conduit structures with high-velocity cores. Although in many situations the relevant structure is the plume stem (steady slender flow originating from a localized source), some works (Moses, Zocchi & Libchaber 1993) have been devoted to the transient frontal structure of the starting plume, often referred to as the *cap*. It turns out that the basic experimental scaling laws found by Moses *et al.* (1993) for the velocity cap also apply to the vertical velocity in the stem (see below and § 5.1).

In the present study, typical Reynolds numbers are small ($Re \sim 10$), owing to the centimetre-scale size of the experimental set-up and the small values of typical velocities. Consequently, we focus here on the case of a steady laminar plume. This problem splits itself into various other subclasses, depending on whether point or extended sources are considered and whether the surrounding medium is bounded or not. The problem of a buoyancy source (point and line) in an unbounded space has been addressed from a theoretical point of view by Yih (1951), Fujii (1963) and Pera & Gebhart (1971) in the particular cases of Prandtl number equal to 1 and 2 (the equivalent dimensionless number we consider here is the Schmidt number S). Worster (1986) proposed an analytical analysis of the laminar steady flow created by a point source (still located in an infinite medium) based on a matching between the inner and outer regions of the plume, and valid for large Prandtl number. Worster's work can be seen as an extension of previous works, as it provides the functional dependence on Prandtl number of the thermal and velocity fields in an axisymmetric laminar plume. More recently, Whittaker & Lister (2006*a*) performed the same kind of calculation, in the case of a semi-infinite medium (no lateral boundaries). Their work is essentially an axisymmetric version of Robert's work (Roberts 1977). Whittaker & Lister (2006*b*) also solved the problem of a steady laminar plume originating from a distributed source (again in a semi-infinite medium). Both of Whittaker and Lister's articles are of great interest for the present study and our results are carefully compared to theirs in the theoretical section of this paper. Umemura & Busse (1989) achieved a very complete theoretical analysis of the axisymmetric laminar flow caused by a temperature difference between the top and bottom walls of a cylinder (free-slip

https://doi.org/10.1017/jfm.2012.641 Published online by Cambridge University Press

hydrodynamic boundary conditions are assumed). This last work is also closely related to the present work and will be exhaustively discussed in the following.

It should be noted that the choice of the dimensionless numbers is closely dependent on the existence of a typical length scale in the problem. In classical convection problems, the Rayleigh number is usually defined as

$$Ra = \frac{\alpha g \Delta\Theta R_c^3}{\nu\kappa}, \tag{1.1}$$

using the size R_c of the extended heat source (in the previous expression, $\Delta\Theta$, α, ν and κ are, respectively, the temperature of the source, the thermal expansion coefficient, the kinematic viscosity and the thermal diffusivity). This will be the case in our paper, although it will be adapted to the chemical convection of carbon dioxide. However, for a point source, R_c tends to 0 and $\Delta\Theta$ tends to $+\infty$, so that the correct non-dimensional parameter is a flux Rayleigh number $\mathscr{R}_f$ used, for instance, by Moses *et al.* (1993), which is proportional to the buoyancy flux. The parameter $\mathscr{R}_f$ is proportional to $Ra\,Nu$, because the Nusselt number is defined as the ratio of convective to diffusive flux of temperature, and the buoyancy is equal to the Rayleigh number multiplied by the temperature in non-dimensional units. This relation is extremely useful when comparing the scalings found in the literature for point and extended sources (cf. § 5.1).

In this paper, we consider an isoviscous axisymmetric chemical plume pouring from the meniscus of a centimetre-sized cylindrical glass tube filled with water, after a sudden rise of the partial pressure of carbon dioxide in the surrounding atmosphere. We emphasize the distributed nature of the source (as CO_2 absorption occurs all over the meniscus), so that natural Rayleigh and Nusselt numbers can be defined (definitions of Nusselt and chemical Rayleigh numbers are given in § 2.2). Materials and methods (numerical and experimental) are depicted in § 2. Section 3 is devoted to the detailed description of the phenomenology. The three main regimes (transient, stationary and aperiodic regimes) are presented, whereas the rest of the paper deals with the stationary regime only. Numerical and experimental results are given in § 4. In § 5, we propose a theoretical model of the plume, which leads to scaling exponents (with respect to the Rayleigh number) for the vertical velocity and plume width.

2. Materials and methods

2.1. *Experimental set-up*

An experimental set-up has been designed in order to characterize the flow induced in a vertical glass tube by a time step of the partial CO_2 pressure in the surrounding atmosphere. This experimental set-up is sketched in figure 1 and described in the following.

A circular glass tube (S) of radius R_c (available radii $R_c = 5,\ 6,\ 8$ and 10 mm) filled with distilled water to a height H is immersed in a square optical tank (OT) (inner dimensions 22 mm × 22 mm × 40 mm) to reduce optical deformations. The whole (S + OT) is placed in a cubic pressure steel cell with 1 cm thick quartz windows for visualization on the side and connections for inlet, outlet, pressure and temperature measurements on the top. Carbon dioxide is brought into the cell from a 200 bar bottle (Air Liquide, France) through a pressure reduction valve (0–50 bar). The inlet rate is adjusted by a control valve V1 and triggered by an electro-valve EV. A second valve V2 is available for purging the cell.

https://doi.org/10.1017/jfm.2012.641 Published online by Cambridge University Press

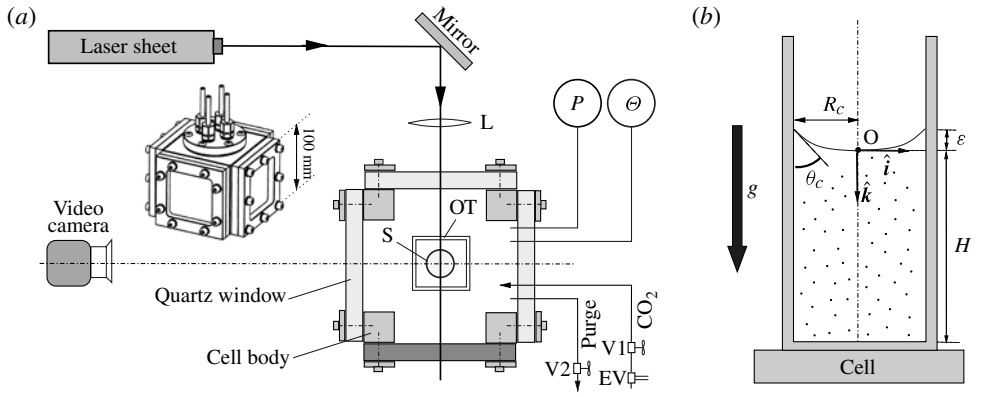


FIGURE 1. Sketch of the experimental set-up. (*a*) Two-dimensional top view of the whole system and (inset) three-dimensional view of the pressure cell. (*b*) Zoom on a two-dimensional side view of the sample (S) itself.

When the electro-valve is opened, the total pressure P rises from $P_0 = 1$ bar up to its final value P_1 in a few tens of seconds. The partial pressure of CO_2 increases from 0 to $P^+ = P_1 - P_0$, which is directly read on a differential manometer (P_0 is the pressure outside the cell). It would be different if the air present in the cell before the experiment was totally replaced by CO_2. During the pressurization, there is a temperature increase of about 30 K, owing to the nearly adiabatic compression of the gas, which damps over a period of 1–2 min. Although this effect influences the initial transient stage, we made sure by varying the duration of the pressurization (and thus the value of the temperature increase) that it does not influence the flow in the stationary regime. The glass tubes are cleaned using 0.5 % Hellmanex–water solution for 12 h, then rinsed out and dried with air. As a result, the contact angle θ_c of the meniscus has been measured from video images and is fairly constant in the interval $[25°, 35°]$.

Particle image velocimetry (PIV) measurements are performed by seeding the fluid with 5 μm diameter polystyrene spheres (Polyscience, USA), whose sedimentation time is much greater than the characteristic time of the experiment. The seeded solution is illuminated at the PIV frequency (8 Hz) following a diametral plane by a red diode laser sheet whose thickness is reduced to 150 μm using a 200 mm focal lens. PIV images are recorded by a 1024 × 1368 Pixelfly video camera (PCO, Germany) equipped with a 50 mm focal lens (Pentax, Japan) and treated by a cross-correlation algorithm detailed in Meunier & Leweke (2003), which leads to a discrete 60 × 60 two-dimensional velocity field.

2.2. *Theoretical and numerical formulation*

As shown in figure 1(*b*), the axis of symmetry of the tube is referred to as $\hat{\boldsymbol{k}}$ and points downwards. The origin O of the reference frame is taken at the extremum of the meniscus, the height of which is referred to as ε. Using the cylindrical coordinates (R, ϕ, Z), the Overbeek–Boussinesq approximation of the Navier–Stokes (NS) equations and the diffusion equation for the carbon dioxide molecular

https://doi.org/10.1017/jfm.2012.641 Published online by Cambridge University Press

concentration C take on the following forms:

$$\frac{\partial \boldsymbol{U}}{\partial T} + (\boldsymbol{U}\cdot\boldsymbol{\nabla})\boldsymbol{U} = -\frac{1}{\rho_0}\boldsymbol{\nabla}P + \alpha C\boldsymbol{g} + \nu\Delta\boldsymbol{U}, \tag{2.1}$$

$$\boldsymbol{\nabla}\cdot\boldsymbol{U} = 0 \tag{2.2}$$

and

$$\frac{\partial C}{\partial T} + (\boldsymbol{U}\cdot\boldsymbol{\nabla})C - D\Delta C = 0, \tag{2.3}$$

where T, $\boldsymbol{U}$ and P are respectively the time, the fluid velocity and the pressure. In the previous equations, $\boldsymbol{g}$ is gravity, ν is the kinematic viscosity (independent of CO_2 concentration), D is the CO_2 diffusivity and α is the chemical expansion coefficient defined by

$$\alpha = \frac{1}{\rho_0}\frac{\partial \rho}{\partial C} \quad \text{or} \quad \rho = \rho_0(1+\alpha C). \tag{2.4}$$

Equations (2.1), (2.2) and (2.3) can be made dimensionless by choosing the radius R_c for typical length, and R_c^2/D, D/R_c and $\rho_0 D^2/R_c^2$ for typical time, velocity and pressure. The saturation concentration at thermodynamic equilibrium $C^+ = K_H P^+$ (where $K_H = 3.4\times10^{-2}$ mol l^{-1} atm^{-1} denotes the Henry's constant of carbon dioxide in water) is naturally chosen as the typical concentration. Using lower-case letters for dimensionless quantities, the NS and diffusion equations can be rewritten as

$$\frac{1}{S}\left[\frac{\partial \boldsymbol{u}}{\partial t} + (\boldsymbol{u}\cdot\boldsymbol{\nabla})\boldsymbol{u} + \boldsymbol{\nabla}p\right] = Ra\, c\,\hat{\boldsymbol{k}} + \Delta\boldsymbol{u}, \tag{2.5}$$

$$\boldsymbol{\nabla}\cdot\boldsymbol{u} = 0 \tag{2.6}$$

and

$$\frac{\partial c}{\partial t} + (\boldsymbol{u}\cdot\boldsymbol{\nabla})\,c - \Delta c = 0. \tag{2.7}$$

In (2.5), S and Ra refer to the Schmidt and Rayleigh numbers, which are defined as

$$S = \frac{\nu}{D} \quad \text{and} \quad Ra = \frac{g\alpha K_H P^+ R_c^3}{D\nu}, \tag{2.8}$$

where P^+ is the partial pressure of CO_2 and R_c is the radius of the tube. In principle, the experimental constants D and ν are known accurately (see e.g. Frank, Kuipers & van Swaaij 1996). However, as our experimental set-up is not thermally regulated, the respective uncertainties on D and ν are determined by the extreme values of room temperature (which only varies by one degree around 293 K). Using data of table 4 in Frank *et al.* (1996) for the diffusion coefficient and dynamic viscosity, and taking into account the variation of the density with the temperature, one finds $D = (1.76\pm0.04)\times10^{-9}$ m^2 s^{-1} and $\nu = 1\pm0.02\times10^{-6}$ m^2 s^{-1}. By contrast, the chemical expansion coefficient α is difficult to measure because the density difference is small (of the order of 0.1 %) at the concentrations considered in this paper. In the literature, the product αK_H has been measured by Hebach, Oberhof & Dahmen (2004), but the results of their measurements are marred by a large uncertainty ($\alpha K_H = 0.004\pm0.001$ MPa^{-1}), which leads to a large uncertainty (of the order of 25 %) in the experimental determination of the Rayleigh number.

The problem must be completed by a suitable set of boundary conditions for the velocity $\boldsymbol{u}$ and the CO_2 concentration c. A no-slip boundary condition at the solid

https://doi.org/10.1017/jfm.2012.641 Published online by Cambridge University Press

walls will be considered, i.e. at $z = h = H/R_c$ and at $r = 1$. Although it would seem obvious to consider a slip boundary condition at the meniscus ($z = z_s(r)$), some experimental and numerical evidence tends to show that it is a no-slip boundary condition, probably due to pollution by surfactants and other substances (Ybert 1998). Both boundary conditions (free-slip and no-slip) at the gas–liquid interface will be used in the numerical simulation. Note that the surface of the meniscus is defined by Concus (1968)

$$\frac{1}{r}\frac{\mathrm{d}}{\mathrm{d}r}\left[\frac{r\,\mathrm{d}z_s/\mathrm{d}r}{\sqrt{1+(\mathrm{d}z_s/\mathrm{d}r)^2}}\right] = Bo\, z_s, \tag{2.9}$$

with $\mathrm{d}z_s/\mathrm{d}r = \cot\theta_c$ at the wall and where the Bond number is defined by $Bo = \rho_0 g R_c^2/\gamma$ ($\gamma = 73$ mN m^{-1} being the surface tension of water in air).

Finally, for the concentration c, there is *a priori* no reason to consider a resistive relation between the mass flux at the interface and the deviation from the gas concentration at saturation. Indeed, all the resistive models presented, for instance, in Cussler (1997), are 'integrated' models, in which processes are considered at a scale much greater than the molecular one. So, we make the assumption that thermodynamic equilibrium is immediately reached at the liquid–gas interface, namely

$$c = 1 \text{ at the interface.} \tag{2.10}$$

The numerical results presented below are obtained by solving equations (2.5), (2.6) and (2.8) completed by the boundary conditions using COMSOL Multiphysics, which is based on a finite element method. The simulations are axisymmetric, with a different surface shape $z_s(r)$ for each Bond number. The mesh, which contains 23 000 elements, is refined at the surface with 10 boundary layer elements with a stretching factor of 1.2, which makes the thickness of the first layer equal to 0.5 % of the tube's radius. This is much smaller than the thickness of the diffusive layer of CO_2, which will be shown to be equal to 2.5 % of the tube's radius at the largest Rayleigh number. The simulations are initiated with $u = c = 0$ inside the fluid.

To summarize, the problem is governed by four dimensionless numbers, h, S, Bo and Ra (we do not consider the contact angle, which is not varied either in the experiments or in the numerics).

3. Phenomenology of the flow

Figure 2 shows three velocity fields obtained experimentally at different times after the pressurization. A temporal animation of the streamlines is also available at http://dx.doi.org/10.1017/jfm.2012.641. The physical process can be divided into three distinct phases, briefly presented in the following. The nature of the observed phenomena and the way they are sequenced is the same for all experiments, although the phases appear at times depending on the Rayleigh number, the Bond number and the aspect ratio. After the pressurization ($t = 0$), CO_2 creates a diffusive layer of dense fluid at the surface, which destabilizes the flow through the Rayleigh–Taylor instability. A plume is formed (figure 2*a*), which propagates downwards to the bottom of the cell. This plume is followed by a few others (typically three or four) at a frequency of the order of 1000 in non-dimensional units, corresponding to a dimensional frequency of 0.05 s^{-1}. This corresponds to the first regime (I), which is very short (of the order of 0.003 in dimensionless time units, corresponding to a dimensional time of 60 s).

After this transient regime, a nearly stationary regime (II) settles in the tube. The plume contains a parallel stem, which fills the whole volume of the cylinder. This

https://doi.org/10.1017/jfm.2012.641 Published online by Cambridge University Press

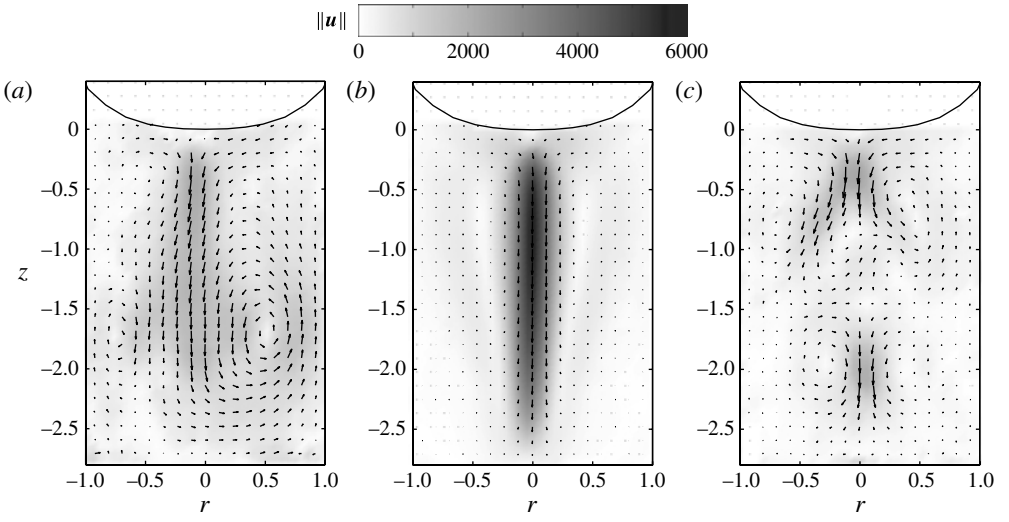


FIGURE 2. PIV velocity fields of the plume in (*a*) the transient regime ($t = 0.003$), (*b*) the stationary regime ($t = 0.012$) and (*c*) the pulsed/aperiodic regime ($t = 0.05$) for $h = 3$, $Bo = 4.9$ and $Ra = 1.9 \times 10^6$, corresponding to $P = 4$ bar, $H = 18$ mm and $R_c = 6$ mm. The value $u = 1000$ corresponds to a dimensional velocity of 0.3 mm s^{-1} and $t = 0.01$ to a dimensional time of 200 s.

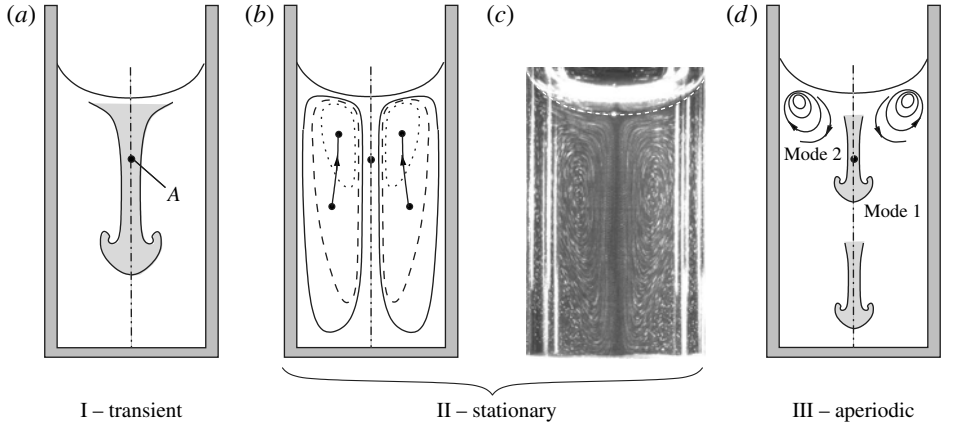


FIGURE 3. (*a*,*b*,*d*) Sketches of the three flow regimes (transient, stationary and aperiodic regimes, respectively). (*c*) Multi-exposure picture of the stationary toroid ($t = 0.003$). In panel (*b*), the trajectory of the 'rotation centres' of the counter-rotating lobes are shown using solid lines (see text for further explanations). Dimensionless numbers $h = 3$, $Bo = 4.9$ and $Ra = 1.9 \times 10^6$, corresponding to $P = 4$ bar, $H = 18$ mm and $R_c = 6$ mm.

parallel and axisymmetric flow is clearly visible in figure 2(*b*), with a large velocity on the axis. Since the bottom of the tube is progressively filled by the saturated solution, the size of the plume, and consequently the vertical extension of the toroid, slowly decreases. At the same time, the 'rotation centre' (the point where the velocity vanishes) of the counter-rotating lobes gets closer to the free surface. This is explained in the sketch of figure 3(*b*), where the streamlines at different times are plotted and

https://doi.org/10.1017/jfm.2012.641 Published online by Cambridge University Press

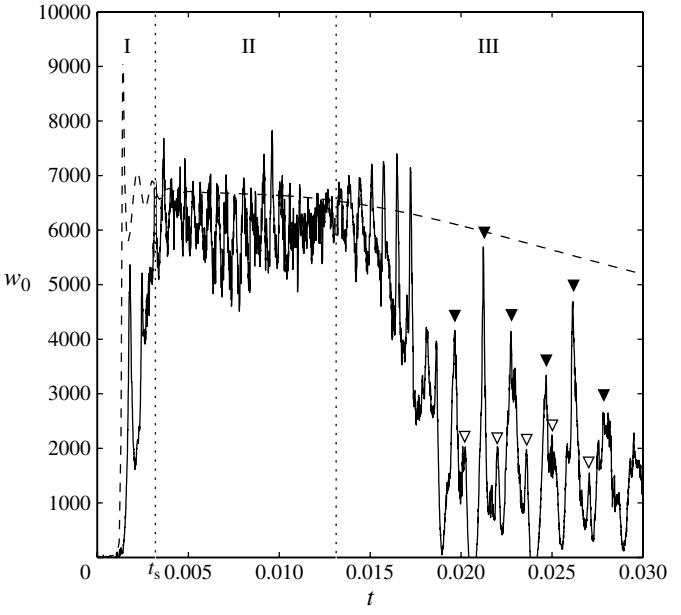


FIGURE 4. Temporal evolution of the axial velocity w_0 measured experimentally (solid line) and obtained numerically (dashed line) at $z = -1$ for $Ra = 1.9 \times 10^6$, $h = 3$, $Bo = 4.9$. Both modes of stage III (open triangles for mode 1, solid triangles for mode 2) are visible. The experiment is performed for $P = 4$ bar, $H = 18$ mm and $R_c = 6$ mm. The vertical velocity reaches its (dimensional) stationary value $W_0 = (D/R_c)w_0 \sim 1.8$ mm s^{-1} at $T = t_s(R_s^2/D) \sim 100$ s.

the motion of the 'rotation centres' are shown with solid lines. This truncation of the plume is a slow process and it appears later as the aspect ratio h is larger. In the following sections of the paper, we will focus on the flow at the beginning of this stationary regime, close to the surface and for a large aspect ratio h, in order to minimize the effect of the bottom.

After a certain period of time, which seems to correspond to the instant when the altitude of the rotation centre is close to $z = 1$, the system enters an aperiodic regime (III) in which plumes pour from the free surface down to the bottom of the sample, as shown in figure 2(*c*). In this stage, two different modes are involved. The first mode (1) consists of a classical plume that falls down from the central region of the interface. The second mode (2) consists of a toroidal flow that arises from the contact line region and grows towards the axis of the tube, finally invading the whole sample (cf. figure 3*d*).

The temporal evolution of the flow is studied by measuring the axial velocity w_0 on the axis, at a depth of one radius ($z = 1$, point A in figure 3). A time sequence of w_0 is presented in figure 4 (solid line). Once again, the general shape of the curve is generic, although the precise velocity amplitude and phase durations depend on the experimental parameters. In the first regime, the velocity amplitude grows rapidly but intermittently, owing to the few plumes (three or four) pouring from the surface. This leads to the second regime, where the amplitude w_0 is nearly constant, although small oscillations are observed (of the order of 10 %, probably due to imperfections of the experiment). Finally, in the third regime, the velocity starts oscillating with an increasing amplitude and suddenly decreases close to 0. This drop is followed by

https://doi.org/10.1017/jfm.2012.641 Published online by Cambridge University Press

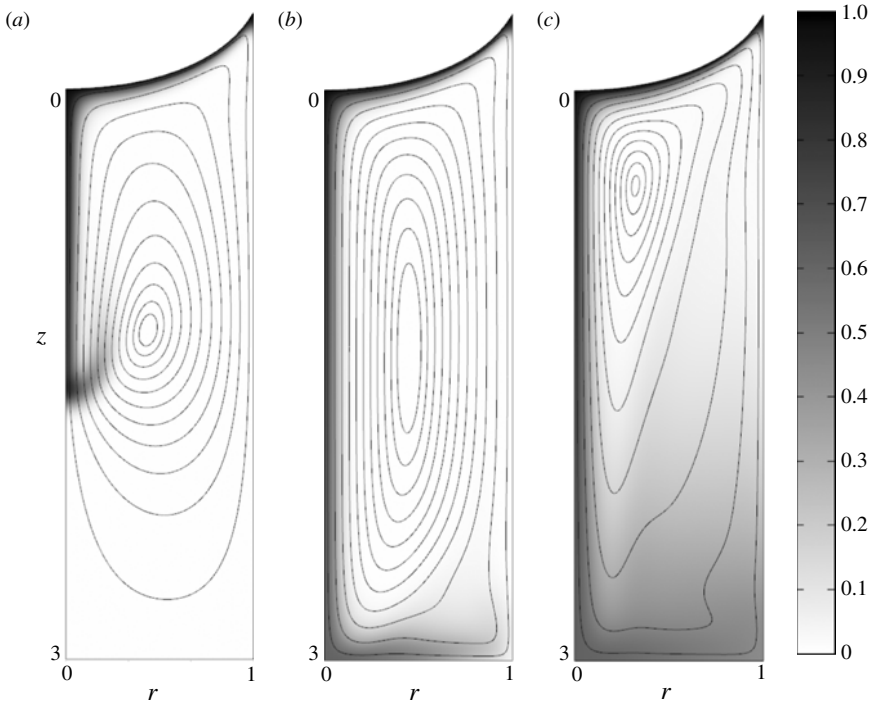


FIGURE 5. Numerical streamlines and density field (greyscale) of the plume in (*a*) the transient regime ($t = 0.0015$), (*b*) the stationary regime ($t = 0.005$) and (*c*) what should be the aperiodic regime ($t = 0.025$) for $h = 3$, $Bo = 4.9$ and $Ra = 1.9 \times 10^6$. Note that the aperiodic regime is not captured numerically (see § 4).

a succession of large and small peaks of velocity corresponding to modes 1 and 2, respectively.

Several runs have been dedicated to the study of the upper hydrodynamic boundary condition. The meniscus has been seeded with PIV markers, which remained at the surface, and a sequence of pictures (∼1000 images) has been taken from above. It clearly showed that the particles did not move between the first and the last image, i.e. during 0.005 dimensionless time units. Moreover, a zoom of the velocity field below the surface showed a small shear layer. As explained before, this is probably due to the effect of the polluting substances coming from the atmosphere or from the PIV particles. As a consequence, numerical simulations have been performed using a no-slip boundary condition at the surface.

Figure 5 shows three density fields and streamlines obtained numerically at the same times and parameters as in the experimental results in figure 2. In the first regime (figure 5*a*), a CO_2-rich transient plume is recovered. In the stationary regime (figure 5*b*), the CO_2 goes down through the tube and spreads on the bottom. At a later time (figure 5*c*), the CO_2 fills a large part of the tube, which reduces the extension of the recirculating flow and raises the 'rotation centre' of the counter-rotating lobes. However, the numerical simulations never exhibited the aperiodic regime III. This is very clear in figure 4, where the velocity amplitude w_0 obtained numerically is plotted as a dashed line: it decreases slowly because the CO_2 fills the tube but never shows oscillations. This is perhaps due to the axisymmetry imposed in the numerics or to

https://doi.org/10.1017/jfm.2012.641 Published online by Cambridge University Press

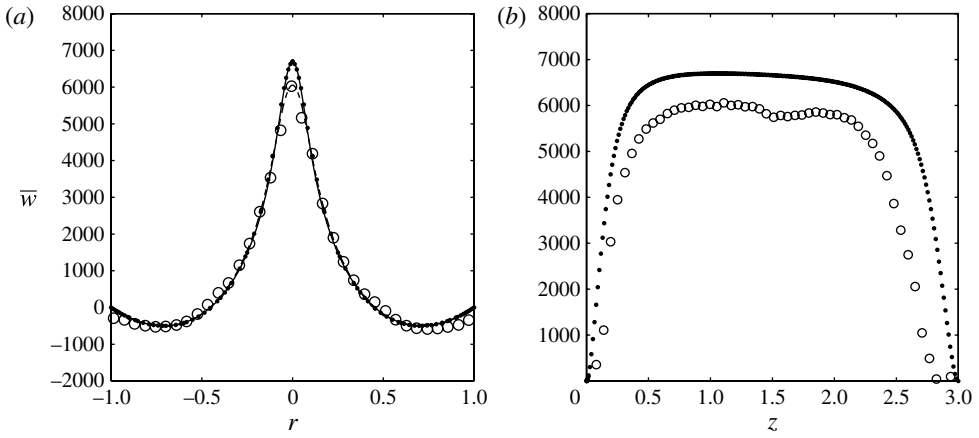


FIGURE 6. Mean profile of vertical velocity at the beginning of the stationary regime as a function of (*a*) r at $z = 1$ and (*b*) z on the axis, for $t = 0.005$, $h = 3$, $Bo = 4.9$ and $Ra = 1.9 \times 10^6$. Numerical results (black dots) are compared to experimental results (open circles). In panel (*a*) solid and dashed lines correspond to the theory-dependent fits (4.1) of the numerical and experimental data, respectively.

the absence of sufficient noise in the numerical simulations such that the flow does not transition from regime II to regime III, although regime II might be unstable. To conclude, although the dynamics of the plume can be divided into three phases, we will only focus on the second (stationary) regime because the first transient regime is dependent on the initial temperature increase and the aperiodic regime III is not rendered numerically. This is the topic of the next sections.

4. Experimental and numerical analysis of the stationary plume

We had several tube sizes at our disposal ($R_c = 5$, 6, 8 and 10 mm, $h = 40$ mm), and the partial pressure of carbon dioxide could be varied from 0 to 14 bar. By varying the radius of the tube, the volume of water and the height of the pressure step, we explored about one decade of aspect ratio ($h \in [1, 8]$ in the experiments and $h \in [0.5, 10]$ in the numerics), one decade of Bond number ($Bo \in [2, 14]$ in the experiments and $Bo \in [2, 30]$ in the numerics) and almost three decades of Rayleigh number ($Ra \in [4 \times 10^5, 10^7]$ in both experiments and numerics). Every quantitative result presented below is related to quantities measured or calculated at $z = 1$.

Typical numerical and experimental profiles of the axial velocity are presented in figure 6. The experimental profiles result from the average of consecutive PIV fields with a duration $\Delta t = 0.002$ taken from the beginning of the stationary stage. Figure 6(*a*) shows the radial profile of velocity, with a thin peak of large velocity on the axis, and a negative (upward) velocity outside the plume due to the recirculation forced by the incompressibility. There is a good agreement between the experiment and the numerics, although the experimental amplitude of the plume is slightly smaller than the numerical amplitude. This appears more clearly in the axial velocity profile (figure 6*b*) with a 10 % difference. However, both results indicate that the amplitude is almost constant as a function of z (at least at the beginning of phase II), except near the surface and the bottom. This indicates that the flow is nearly parallel. This comes from the fact that the distance of radial diffusion $\sqrt{DH/W}$ (W being the

https://doi.org/10.1017/jfm.2012.641 Published online by Cambridge University Press

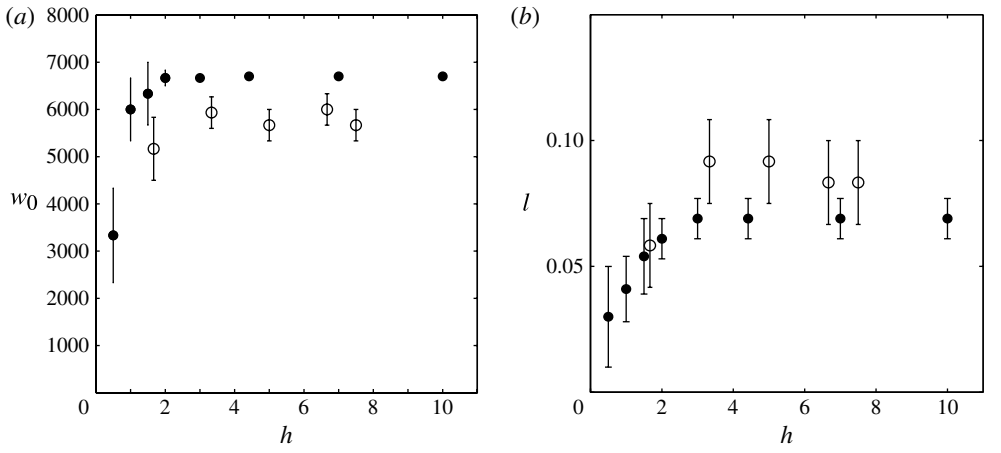


FIGURE 7. (*a*) Vertical velocity and (*b*) width of the convective plume as a function of the aspect ratio obtained one radius below the surface ($z = 1$). Experimental (○) and numerical (●) results; $Bo = 4.9$, $Ra = 1.9 \times 10^6$.

dimensional vertical velocity) is small compared to the radius R_c. This leads, when using dimensionless quantities, to the relation $h \ll Pe$, where the Péclet number is defined as $Pe = W R_c/D = w_0$. Knowing that $W > 10^{-4}$ m s^{-1} in our experiments, the Péclet number is at least of order 1000, which is always greater than h (which lies in the range [1, 10]).

The radial profile of velocity (figure 6*a*) is very well fitted by the profile

$$w_{th}(r) = w_0 \frac{F_l(r)}{F_l(0)}, \tag{4.1}$$

where

$$F_l(r) = \int_{r/l}^{1/l} \frac{1 - \mathrm{e}^{-x^2}}{x}\,\mathrm{d}x + (r^2 - 1)(1 - l^2), \tag{4.2}$$

which is a simplified form of the exact solution of the NS equations given in the next section (equations (5.7) and (5.8)) and obtained for a parallel axial flow of amplitude w_0 and a Gaussian concentration profile of width l. Note that the choice of a Gaussian concentration profile is strongly suggested by Whittaker & Lister (2006*a*), who proved that the concentration profile inside a plume is Gaussian at leading order, and by Schlien & Boxman (1979), whose experimental profiles are clearly Gaussian.

For each experimental run and numerical calculation, the plume widths and amplitudes are obtained by fitting the average profile $\overline{w}(r)$ using the theoretical form $w_{th}(r)$, where both parameters l and w_0 are free.

The experimental and numerical parameters w_0 and l are plotted with respect to the aspect ratio in figure 7. For aspect ratios larger than 2, both quantities are independent of h, which is consistent with the fact that the flow is parallel and nearly independent of z. It should be noted that the experimental velocity w_0 is always smaller (10 %) than in the numerics and the size l of the plume is always larger in the experiments than in the numerics. The drop in velocity and size observed for $h < 2$ (see figure 7*a*) is due to the short duration of the stationary stage. Indeed, in experiments with a small aspect ratio, the system falls almost immediately into the aperiodic regime III. In the

https://doi.org/10.1017/jfm.2012.641 Published online by Cambridge University Press

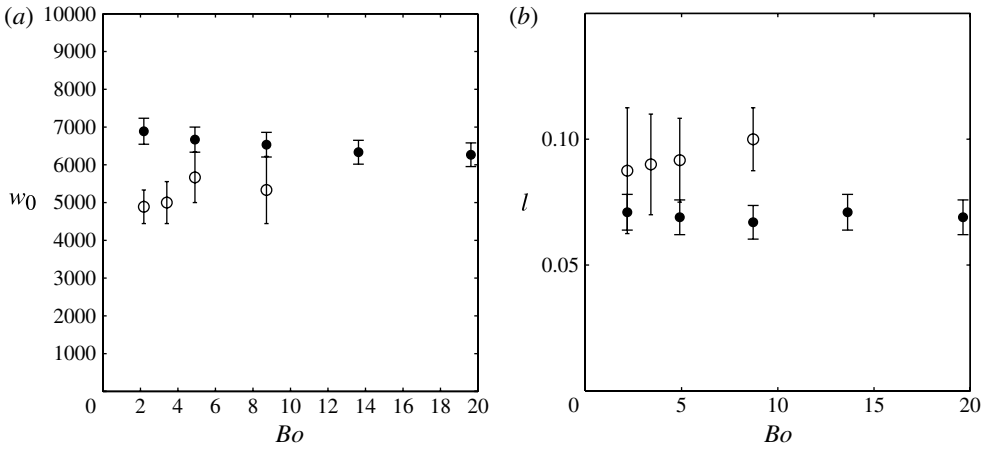


FIGURE 8. (*a*) Vertical velocity and (*b*) width of the convective plume as a function of the Bond number obtained one radius below the surface ($z = 1$). In the numerics (•), $h = 10$. In the experiments (○), $h = 6.5,\ 5.2,\ 4.5$ and 3.3 for $Bo = 2.2,\ 3.4,\ 4.9$ and 8.7, respectively. Rayleigh number $Ra = 1.9 \times 10^6$.

numerics, the CO_2 quickly fills the tube, leading to the vanishing of the plume. In the following, we will thus focus our study on aspect ratios larger than 2.

The Bond number can be varied at a fixed Rayleigh number by varying the radius of the sample R_c simultaneously with the pressure (as R_c^{-3}). A variation of the Bond number has almost no effect on the characteristics of the stationary stage, which is illustrated in figure 8. Indeed, w_0 and l vary by less than 10 % when the Bond number increases from 2 to 20. This suggests that the buoyancy force created at the free surface (which is tilted in the meniscus) is much smaller than the buoyancy force within the vertical plume. Experiments could not be performed at large Bond numbers because they corresponded to a large radius and thus to a small aspect ratio h (due to the limited height of the cell), where the stationary regime is very short.

Concerning the effects of h and Bo, the observations can be summarized as follows: provided the stationary stage exists, the two parameters have no effect on its characteristics.

The variations of w_0 and l with respect to the Rayleigh number Ra are presented in figure 9 and seem to collapse onto the same power curve, whatever the Bond number and the aspect ratio. Concerning the velocity amplitude, the agreement between experiments and numerics is fairly good even if the numerical velocity is slightly larger than the experimental velocity (∼5 %). This may come from the PIV method, which tends to underestimate the peaks of velocity, and from the uncertainty on the experimental Rayleigh number (which is of the order of 25 % as explained in § 2.2). The numerical results are properly fitted by a power-law function with an exponent equal to 0.72. The latter is very close to the one obtained by fitting to the experimental results (0.72 ± 0.03).

The numerical width l plotted as a function of the Rayleigh number is 20 % lower than the experimental results. This systematic discrepancy might come from the fitting method that we used. Indeed, a slight difference in w_0 between numerical and experimental velocities results in a greater relative difference in l. Despite this defect, a power-law exponent of -0.28 enables a good fit of the numerical data.

https://doi.org/10.1017/jfm.2012.641 Published online by Cambridge University Press

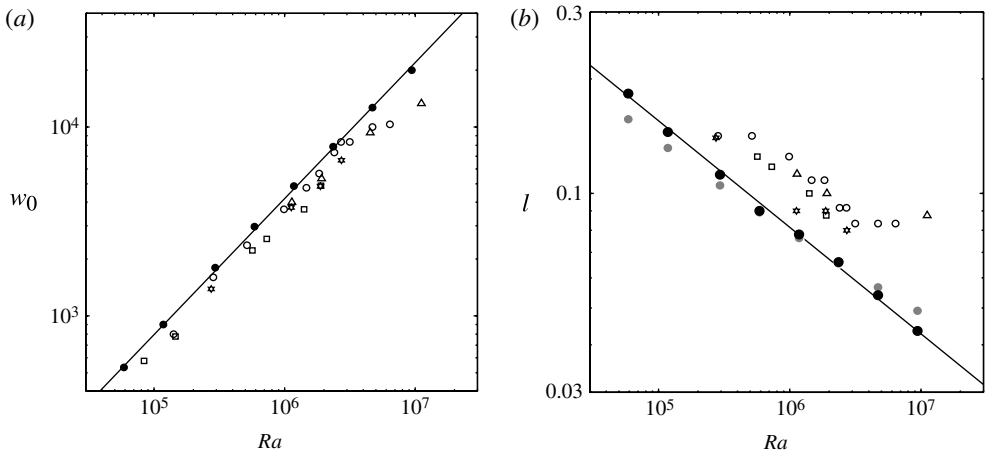


FIGURE 9. (*a*) Vertical velocity and (*b*) width of the convective plume as a function of the Rayleigh number one radius below the surface ($z = 1$). Experimental results are obtained at: $Bo = 2.2$, $h = 6.5$ (□); $Bo = 3.4$, $h = 5.2$ (∗); $Bo = 4.9$, $h = 4.5$ (○); and $Bo = 8.7$, $h = 3.3$ (△). Numerical results are obtained at $Bo = 4.9$, $h = 4.5$, with a no-slip condition at the surface (•). Solid lines correspond to a fit of the numerical data. In panel (*b*), grey symbols correspond to the Gaussian size of the concentration profile $c(r)$ and black symbols to the size obtained by fitting the profile of velocity w with $w_{th}(r)$.

l				w_0			δ_c			δ_u
exp.	num.		theor.	exp.	num.	theor.	num.		theor.	num.
	slip	no-slip					slip	no-slip		
−0.23	−0.23	−0.26	−0.21	0.72	0.72	0.69	−0.27	−0.20	−0.28	−0.2

TABLE 1. Summary table of all the apparent exponents resulting from the fit of experimental (exp.), numerical (num.) and theoretical (theor.) results by power laws. The numerical exponent found for w_0 is valid for slip and no-slip boundary conditions.

This exponent is also close to the one obtained by fitting the experiments only (-0.23 ± 0.07). In figure 9(*b*), grey solid circles correspond to the value of l obtained by fitting the numerical concentration profile with a Gaussian function. Although the order of magnitude is not altered, the power-law exponent is ∼15 % greater. So, even if the two fitting methods are not strictly equivalent, a power-law exponent of about ~ -0.26 is satisfactory in every case.

All the values of the different exponents mentioned above are gathered in table 1.

5. Theoretical model

This section intends to give a simplified model of the plume created by CO_2 diffusion across the surface. The curvature of the meniscus and the finite height of the tube are neglected since it was shown in the last section that the flow is independent of the Bond number and the aspect ratio (for $Bo > 2$ and $h > 2$). The flow is thus

https://doi.org/10.1017/jfm.2012.641 Published online by Cambridge University Press

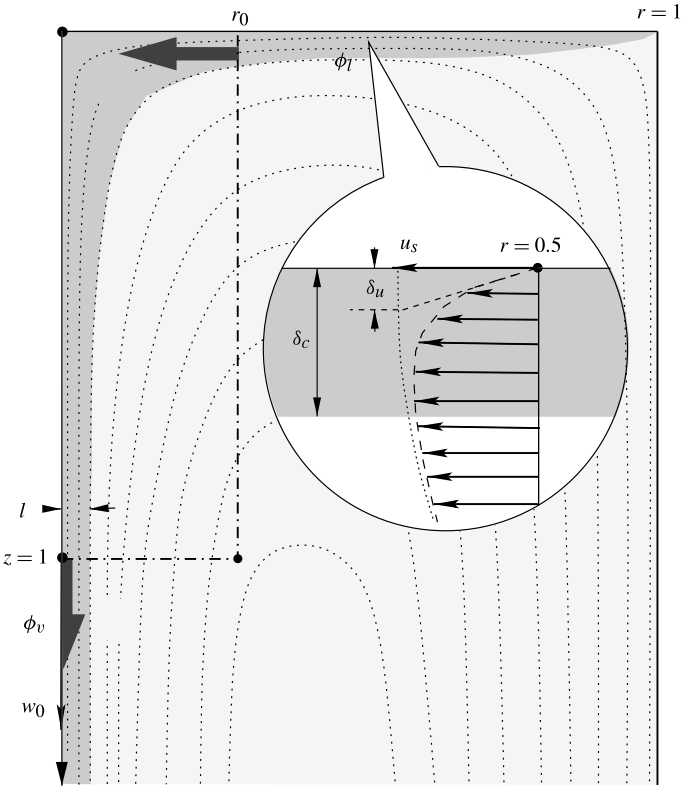


FIGURE 10. Explanatory sketch of the theoretical section. Here l and w_0 denote the lateral size of the concentration profile and the maximum velocity in the plume (at $z = 1$). The concentration thicknesses δ_c and velocity profile at the surface are specified on a magnification of the region located close to the surface. The no-slip velocity profile is drawn with a dashed line. The free-slip velocity profile is drawn with a dotted line and defines the velocity at the surface u_s. In the stationary regime, the vertical and lateral fluxes ϕ_v and ϕ_l are equal.

modelled by a velocity u_s on a flat free surface, which sinks on the axis and becomes parallel for large z, as sketched in figure 10. The diffusing layer of CO_2 has a thickness δ_c beneath the surface and is advected into a plume of characteristic size l and maximum velocity w_0. Two different boundary conditions are considered at the surface. In § 5.2 a free-slip boundary condition creates a velocity profile drawn as a dotted line in figure 10. In § 5.3 a no-slip boundary condition creates a velocity profile drawn as a dashed line in figure 10. First, scaling laws are derived in § 5.1.

5.1. *Scaling laws*

In this paper, we need to give a model for a plume connected to a diffusing free surface of finite size. This is slightly different from previous theoretical models, which were mostly adapted to point sources with a finite flux of buoyancy (except for Whittaker & Lister 2006*b*). In these classical models, the size of the plume increases proportionally to z as a result of the diffusion of c. In our experiments, this expansion of the plume is small because the aspect ratio is smaller than the Péclet number (as already stated above). As a consequence, the advection term on the left of (2.5)

https://doi.org/10.1017/jfm.2012.641 Published online by Cambridge University Press

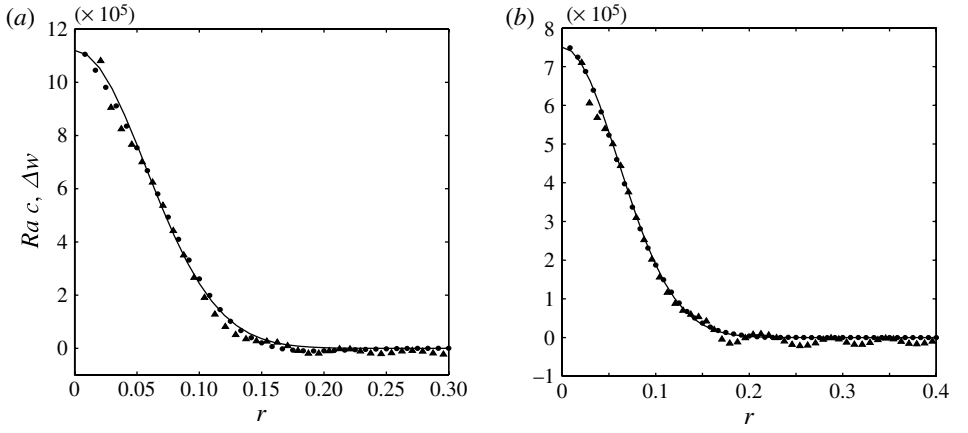


FIGURE 11. Radial profile of the gravity term $Ra\,c$ (•) and the viscous term Δw (▲) for the axial stationary flow, in the numerical simulations, for $h = 4.3$, $Bo = 4.9$, $Ra = 1.17 \times 10^6$. The boundary conditions at the interface are (*a*) free-slip and (*b*) no-slip. Solid lines correspond to Gaussian fits. The quantities are taken at the very beginning of phase II ($t = 0.005$) and are calculated at $z = 1$.

is small because the flow is nearly parallel. It means that the buoyancy force $c\,Ra$ (right-hand side of (2.5)) is balanced by the viscous term Δw. This is confirmed by the numerical simulations, as shown in figure 11, where the two terms (plotted as circles and triangles) are almost equal within the plume. A major consequence of this classical assumption is that the characteristic velocity of the plume w_0 thus scales as

$$w_0 \sim Ra\, l^2, \tag{5.1}$$

l being the characteristic size of the plume (it is recalled that the concentration is equal to 1 at the surface). Another relation can be found by calculating the vertical flux of concentration ϕ_v, which scales as $w_0 l^2$ in the plume. In the stationary regime, this flux is equal to the incoming lateral flux ϕ_l entering a cylindrical surface of radius r_0 close to the axis (dot-dashed line in figure 10), namely

$$\phi_l \sim 2\pi r_0 u_s \delta_c, \tag{5.2}$$

where δ_c is the thickness of the diffusive layer of concentration and u_s is the radial velocity in the close vicinity of the surface; δ_c is proportional to the square root of the time $\tau \sim 1/u_s$ spent by the fluid particles at the surface. We can further assume that the velocity at the surface u_s is proportional to w_0 if the structure of the recirculating flow within the cell is independent of the Rayleigh number. This assumption seems relevant in the scope of a creeping flow. As a consequence, the incoming flux ϕ_l at the surface scales as $\sqrt{w_0}$. It should be noted that matching between the bulk and the plume requires taking $l \ll r_0 \ll 1$. However, it will be shown that the product $r_0\delta_c$ is independent of the radius when r_0 tends to 0. So, equating ϕ_v and ϕ_l gives the second relation

$$w_0 \sim l^{-4}. \tag{5.3}$$

Relations (5.1) and (5.3) lead to the following pair of scaling laws:

$$l \sim Ra^{-1/6} \quad \text{and} \quad w_0 \sim Ra^{2/3}. \tag{5.4}$$

https://doi.org/10.1017/jfm.2012.641 Published online by Cambridge University Press

These predictions are in fairly good agreement with the numerical and experimental results, for which the exponents were equal to -0.23 for the size and 0.72 for the velocity. They are also strictly identical to those derived by Whittaker & Lister (2006*b*) in the free-slip case, for a semi-infinite medium. It should be noted that, at first glance, scaling law (5.4) for the velocity seems different from the classical scaling law $w_0 \sim \mathscr{R}_f^{1/2}$ found for a point source (Moses *et al.* 1993). However, the latter is also valid because the flux Rayleigh number is defined using the buoyancy flux. We recall that $\mathscr{R}_f = Nu\,Ra$. As the dimensionless flux ϕ $(= \phi_v = \phi_l)$ is strictly equivalent to the mass transfer Nusselt number (i.e. $Nu = \phi \sim w_0 l^2$), then $\mathscr{R}_f \sim Ra^{4/3}$, so that the velocity amplitude w_0 finally scales as $\mathscr{R}_f^{1/2}$. The previous considerations lead to the scaling law for the mass transfer Nusselt number (also called the Sherwood number)

$$Nu \sim Ra^{1/3}.$$

This is larger than the scaling $Nu \sim \mathscr{R}_f^{0.12}$ (or $Nu \sim Ra^{0.14}$) found in the experiment of Moses *et al.* (1993) for a thermal plume created by a point source.

5.2. *Gaussian plume with free-slip boundary condition at the surface*

We now wish to give a more accurate description of the flow. It can be seen in figure 11 that the concentration is very close to Gaussian (plotted as a solid line). This assumption is in agreement with experimental results in the literature (Schlien & Boxman 1979) and it can even be shown theoretically (Whittaker & Lister 2006*a*) that the profile is Gaussian at first order in $1/S$. Moreover, for a slip boundary condition at the surface (see figure 11*a*), the concentration is very close to 1 at $r = 0$ (here $Ra = 1.7 \times 10^6$). This means that the concentration profile is properly rendered by

$$c(r) = \exp(-r^2/l^2), \tag{5.5}$$

l being the lateral size of the plume. This assumption is not fully valid for a no-slip boundary condition at the surface: even though the plume is still Gaussian, the maximum concentration is lower than 1 (see figure 11*b*). The necessary correction that must be applied to the model to render this drop will be presented in § 5.3. We first describe the model for a slip boundary condition at the upper surface.

Assuming, as previously, that the flow is stationary and parallel implies that the terms $\partial_t \boldsymbol{u}$ and $\boldsymbol{u} \cdot \boldsymbol{\nabla} \boldsymbol{u}$ can be neglected in the Navier–Stokes equation (2.5), leading to a set of equations consistent with a Stokes flow. The problem is then equivalent to one where the lubrication approximation is applied. The lubrication assumption is even more justified at large Schmidt number since these two terms are divided by S. It seems natural to neglect the pressure term because it is also divided by the Schmidt number. But, in fact, the pressure term is necessary, as it creates the recirculating flow outside of the plume. This term is actually responsible for the small difference between the terms $c\,Ra$ and Δw, the latter being slightly negative outside of the plume, as can be seen in figure 11. However, the radial component of the Navier–Stokes equation (2.5) indicates that the pressure is independent of r (since the flow is parallel) such that the vertical pressure gradient is a constant $\partial_z p = K$. With these two assumptions, the vertical component of the Navier–Stokes equation (2.5) simply takes the form

$$\frac{1}{r}\frac{\partial}{\partial r}\left(r\frac{\partial w}{\partial r}\right) = \frac{K}{S} - Ra\,c. \tag{5.6}$$

https://doi.org/10.1017/jfm.2012.641 Published online by Cambridge University Press

This equation can be integrated using the profile of concentration (5.5) and the boundary conditions $\partial_r w(0) = 0$, $w(1) = 0$, which leads to

$$w(r) = \frac{Ra\, l^2}{2} \int_{r/l}^{1/l} \frac{1 - \mathrm{e}^{-r'^2}}{r'} \,\mathrm{d}r' + \frac{K}{4S}(r^2 - 1). \tag{5.7}$$

The incompressibility of the fluid means that the mass flux $\int rw(r)\,\mathrm{d}r$ vanishes, allowing for the determination of the pressure gradient K, which can be written (after an integration by parts) as

$$K = \frac{\partial p}{\partial z} = 2\, Ra\, S\, l^2[1 - l^2(1 - \mathrm{e}^{-l^{-2}})]. \tag{5.8}$$

For small l, the velocity profile is thus equal to the velocity profile used to fit the experimental and numerical data, with an amplitude w_0 equal to

$$w_0 = Ra\, l^2 F_l(0)/2, \tag{5.9}$$

where

$$F_l(r) = \int_{r/l}^{1/l} \frac{1 - \mathrm{e}^{-x^2}}{x} \,\mathrm{d}x + (r^2 - 1)[1 - l^2(1 - \mathrm{e}^{-l^{-2}})]. \tag{5.10}$$

It should be noted that the first term can be made explicit using the exponential integral function $E_i(x) = \int_x^\infty \mathrm{e}^{-t}\,\mathrm{d}t/t$. This term is then similar to the profile obtained by Worster (1986) and Whittaker & Lister (2006*a*) inside the plume, in the case of a radially infinite medium. The second term corresponds to the recirculation, which appears in this confined geometry through the pressure term. This term becomes logarithmically small compared to the first term when l tends to 0. Equation (5.9) corresponds to the scaling given in (5.1), where the prefactor is made explicit. Note that $F_l(0)$ can be approximated at small l by

$$F_l(0) = -\log(l) + (\tfrac{1}{2}\Gamma - 1) + l^2 + o(e^{-l^{-2}}), \tag{5.11}$$

where $\Gamma \simeq 0.5772$ is the Euler constant. As we did in § 5.1, the next step is to calculate the vertical flux of concentration in the plume:

$$\phi_v = \int_0^1 2\pi r' w(r') c(r')\,\mathrm{d}r' = \tfrac{1}{2}\pi\, Ra\, l^4 G_l. \tag{5.12}$$

Here the function G_l can be calculated using the velocity profile (5.7), and simplified by integrating by parts, which leads to

$$G_l = \int_0^{1/l} \frac{(1 - \mathrm{e}^{-r'^2})^2}{r'} \,\mathrm{d}r' - [1 - l^2(1 - e^{-l^{-2}})]. \tag{5.13}$$

In addition, G_l can also be approximated at small l by

$$G_l = -\log(l) + \left(\frac{\Gamma - \ln 2}{2} - 1\right) + 2l^2 - l^4 + o(e^{-l^{-2}}). \tag{5.14}$$

The final step consists of calculating the flux of concentration at the surface. The velocity at the surface can be obtained analytically by solving the Navier–Stokes equations in the limit of low Reynolds number in the cylindrical cavity (Duda & Vrentas 1971). Following Umemura & Busse (1989), the velocity field outside

https://doi.org/10.1017/jfm.2012.641 Published online by Cambridge University Press

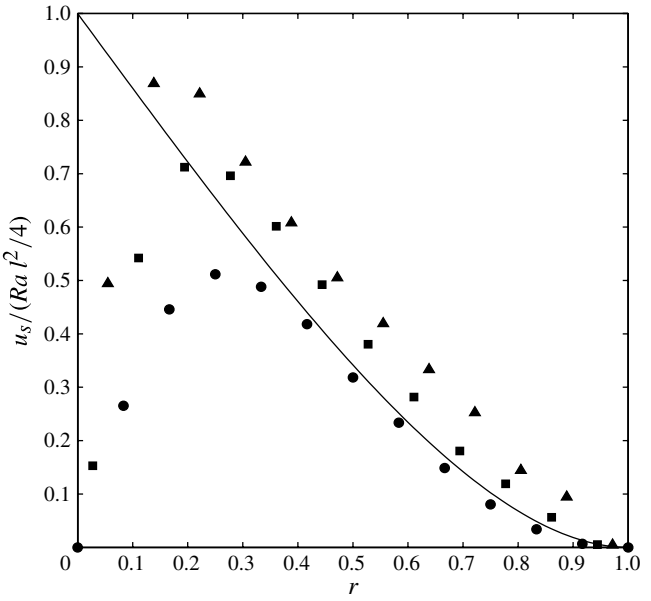


FIGURE 12. Radial profile of tangential velocity at the surface obtained numerically for a slip boundary condition for $Bo = 19.6$, $h = 5$ and $Ra = 5 \times 10^4$ (•), $Ra = 2 \times 10^5$ (■) and $Ra = 2 \times 10^6$ (▲). The solid line corresponds to the analytical profile given by (5.15).

the plume can be expanded in a Fourier series $\Sigma \sin(n\pi z/h) f_n(r)$ and matched asymptotically at small r with the solution inside the plume (which is not valid close to the surface). This series is valid for all z outside of the plume and can be approximated for small z to

$$u_s(r) = -\frac{Ra\,l^2}{4}\left(1 + \sum_{k=0}^{+\infty} \beta_k r^{2k+1}\right). \tag{5.15}$$

The detail of the calculation is given in the appendix, leading to an analytic form of the coefficients β_k given by (A 15), which converge rapidly. The first five coefficients are equal to $\beta_0 = -1.4030$, $\beta_1 = 0.3322$, $\beta_2 = 0.0518$, $\beta_3 = 0.0136$ and $\beta_4 = 0.0038$. This prediction, which is plotted in figure 12 as a solid line, is in excellent agreement with the numerical result outside the plume core. The numerical velocity is slightly above the theoretical velocity for large Rayleigh numbers. This is probably due to a weak effect of the meniscus, whose slope tends to accelerate the layer of dense fluid at the surface. It should be noted that this velocity profile is different from the one derived theoretically by Whittaker & Lister (2006*b*) because they considered the case of an infinite domain along r. Since the diffusive thickness δ_c is small, the radial component of the velocity is independent of z in the diffusive layer so that the incompressibility condition and the boundary condition $w = 0$ at the surface allows the vertical velocity to be calculated as

$$w_s(r, z) = -\frac{z}{r}\frac{\partial(ru_s)}{\partial r}. \tag{5.16}$$

Introducing the velocity field (u_s, w_s) into the equation for the concentration (2.8), and assuming that the gradients along r are negligible compared to those along z in the

https://doi.org/10.1017/jfm.2012.641 Published online by Cambridge University Press

viscous term, leads to

$$u_s \frac{\partial c}{\partial r} - \frac{z}{r}\frac{\partial (r u_s)}{\partial r}\frac{\partial c}{\partial z} = \frac{\partial^2 c}{\partial z^2}, \tag{5.17}$$

with the boundary conditions $c = 1$ at $z = 0$ and $c = 0$ at $z = +\infty$. As shown by Whittaker & Lister (2006*b*), searching for a self-similar solution $\hat{c}(\zeta)$ depending only on the rescaled height $\zeta = z/\delta_c(r)$ leads to a very simple equation $\hat{c}'' + 2\zeta\hat{c}' = 0$ if the concentration thickness satisfies

$$\begin{aligned}\delta_c(r) &= \frac{2}{r u_s}\left(\int_1^r r'^2 u_s(r')\,\mathrm{d}r'\right)^{1/2} \\ &= \frac{4}{rl\sqrt{Ra}}\frac{\left[\frac{1}{3}(1-r^3) + \sum \dfrac{\beta_k}{2k+4}(1-r^{2k+4})\right]^{1/2}}{1 + \sum \beta_k r^{2k+1}}.\end{aligned} \tag{5.18}$$

Using the boundary conditions, the concentration field can finally be written as

$$c(r, z) = 1 - \mathrm{erf}\left[\frac{z}{\delta_c(r)}\right]. \tag{5.19}$$

This solution is plotted in figure 13(*a*) as a solid line and shows an excellent agreement with the numerical result. The numerical profile can actually be fitted by an error function (dotted line) to measure the thickness δ_c for each Rayleigh number. The value of δ_c taken from numerical calculations is plotted in figure 13(*b*) as circles. It scales as $Ra^{-0.27}$ and is very close to the theoretical prediction, which is plotted as a solid or dashed line depending on whether l is taken from the numerics or from the theory.

It should be noted that this solution respects the correct boundary conditions at $r = 1$, although the tangential velocity vanishes. Close to the plume (i.e. for r tending to 0), the flux can be calculated assuming that $u(z')$ is equal to u_s given by (5.15) such that

$$\phi_l = \int_0^{+\infty} 2\pi r u(z') c(z')\,\mathrm{d}z' = \pi l Q\sqrt{Ra}, \tag{5.20}$$

where

$$Q = 2\sqrt{\frac{1}{3} + \sum_{k=0}^{+\infty}\frac{\beta_k}{2k+4}}\int_0^{\infty}[1 - \mathrm{erf}(z')]\,\mathrm{d}z' = 0.2426. \tag{5.21}$$

The result (5.20) is in agreement with the scaling $\phi_l \sim \sqrt{w_0}$ because $l\sqrt{Ra}$ is proportional to $\sqrt{w_0}$. Note also that the result does not depend on the radius at small r. Again equating the fluxes (5.12) and (5.20) and using the velocity w_0 given by (5.9) on the axis leads to the final result for the size l and the velocity w_0 of the plume:

$$l = \left(\frac{2Q}{G_l}\right)^{1/3} Ra^{-1/6}, \tag{5.22}$$

$$w_0 = \left(\frac{Q}{\sqrt{2}G_l}\right)^{2/3} F_l(0) Ra^{2/3}. \tag{5.23}$$

https://doi.org/10.1017/jfm.2012.641 Published online by Cambridge University Press

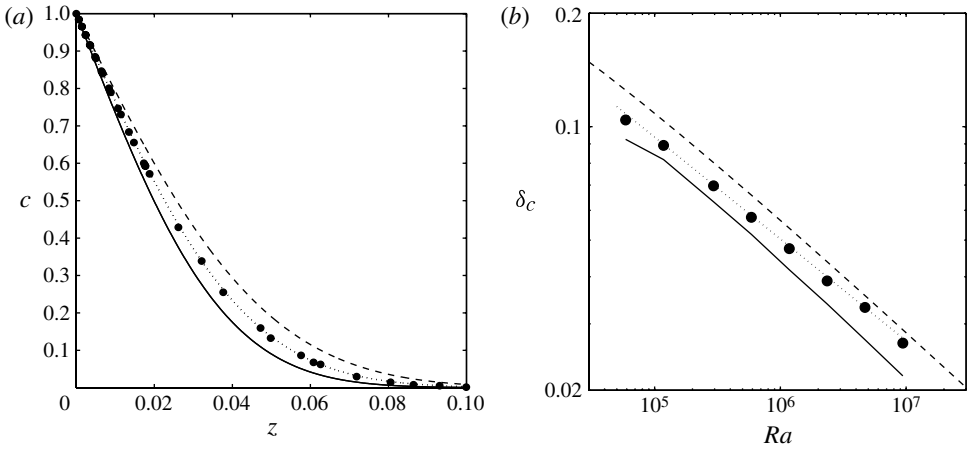


FIGURE 13. (*a*) Numerical profiles of concentration as a function of z below the surface in the case of free-slip boundary conditions for $Ra = 1.17 \times 10^6$. (*b*) Variation of the chemical boundary layer thickness δ_c with the Rayleigh number. Symbols are the numerical results. Solid lines correspond to the exact theoretical predictions (5.18) and (5.19), where l is taken from the numerical data. Dashed lines correspond to the exact theoretical predictions (5.18) and (5.19), where l is given by the theory (5.22). Dotted lines correspond to a fit using (5.19) in panel (*a*) and to a fit as a power law $Ra^{-0.27}$ in panel (*b*). Here, $r = 0.5$, $h = 3$ and $Bo = 4.9$.

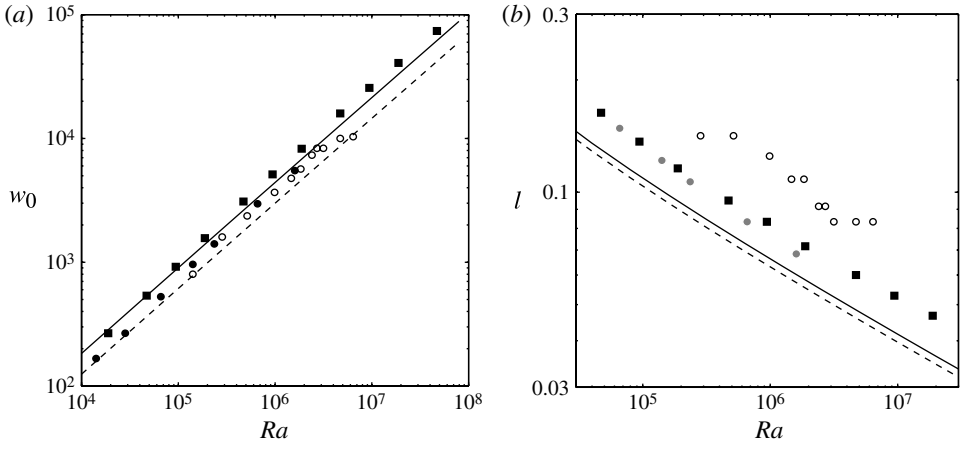


FIGURE 14. (*a*) Vertical velocity and (*b*) width of the convective plume one radius below the surface as a function of the Rayleigh number. Symbols correspond to experimental results (○) and to numerical results for no-slip boundary conditions (●) and slip boundary conditions (■). The theoretical predictions (5.22) and (5.23) are plotted with solid lines for the slip boundary conditions and dashed lines for the no-slip boundary conditions. In the numerics $Bo = 19.6$, $h = 5$; and in the experiments $Bo = 4.9$, $h = 4.5$.

The prediction for the velocity amplitude, plotted as a solid line in figure 14(*a*), is in excellent agreement with the numerical results for a slip boundary condition (plotted as filled squares). The agreement for the width of the plume (plotted in figure 14*b*) is not as good, but the theory still predicts the correct slopes. It is recalled that there is

https://doi.org/10.1017/jfm.2012.641 Published online by Cambridge University Press

no adjustable parameter in this theory, which could explain this discrepancy. It should also be noted that the logarithmic dependence of $F_l(0)$ and G_l makes (5.22) solvable numerically only. However, by using (5.11) and (5.14), one can straightforwardly calculate the corrective logarithmic factor that is to be applied to the scaling laws (5.4) and find

$$w_0 \sim 0.170\, Ra^{2/3}\,(\ln Ra)^{1/3} \quad \text{and} \quad l \sim 1.428\, Ra^{-1/6}\,(\ln Ra)^{-1/3}\,. \tag{5.24}$$

This logarithmic dependence explains the fact that the slope increases slightly with the Rayleigh number in figure 14(*b*), which is in excellent agreement with the numerical result. In the previous expressions, the logarithmic factors slightly modify the scaling laws and explain the small difference between the scaling exponents given by the model in § 5.1 and the exponents obtained by fitting the numerical simulations. Indeed, fitting the theory for Ra between 10^4 and 10^8 gives apparent exponents equal to 0.69 and -0.21, in very good agreement with the numerical exponents equal to 0.72 and -0.21.

The concentration thickness δ_c can also be calculated theoretically using (5.18) and is plotted in figure 13(*b*). There is an excellent agreement with the numerical result. The thickness scales as $(Ra/\ln Ra)^{-1/3}$, which gives an apparent exponent equal to -0.28, very close to the exponent -0.27 found numerically.

Finally, this leads to a scaling law for the mass Nusselt number that is equal to the buoyancy flux ϕ_l (since R_c and R_c^2/D are taken as length and time scales)

$$Nu \sim 1.09\,(Ra/\ln Ra)^{1/3}\,. \tag{5.25}$$

Note that this scaling law is similar to the one obtained by Whittaker & Lister (2006*b*) in the case of a distributed source, in a semi-infinite medium and for a free-slip boundary condition at the surface. However, it is three times smaller in our radially confined geometry than in their radially open case.

5.3. *No-slip boundary condition*

We do not pretend, in this section, to give a rigorous theoretical picture of the corrections induced by the no-slip boundary condition. We just try to identify the dominant effects that provoke a 30 % drop in the velocity amplitude.

In fact, the main effect of the no-slip condition on $z = z_s$ is to modify the profile of velocity at the surface (see figures 10 and 15). The shear layer so created weakens the mass flux, which leads to the observed decrease in velocity. As shown in figure 15, the velocity profile inside the shear layer can be properly fitted by an error function

$$u(z) = u_s\,\mathrm{erf}(z/\delta_u), \tag{5.26}$$

where u_s is still given by the law (5.15) as in the free-slip case. Note that we do not use the term 'viscous boundary layer' to refer to the profile of velocity underneath the surface, for the local Reynolds number is very small ($Re < 0.1$). We use, instead, the term 'surface shear layer', as we think this no-slip velocity profile does not result from a diffusive process. It is surprising to see that the thickness δ_u of the surface shear layer is smaller than the thickness δ_c of the concentration layer, although the kinematic viscosity is three orders of magnitude larger than the diffusivity of the concentration. This probably comes from the confined geometry, which forces the flow close to the surface and thus weakens the size of the surface shear layer. As a consequence, the surface shear layer has a very small effect on the diffusion problem. Thus the concentration profile $c(z)$ is still well fitted by an error function (5.19). The latter is plotted in figure 15(*a*) as a dashed line.

https://doi.org/10.1017/jfm.2012.641 Published online by Cambridge University Press

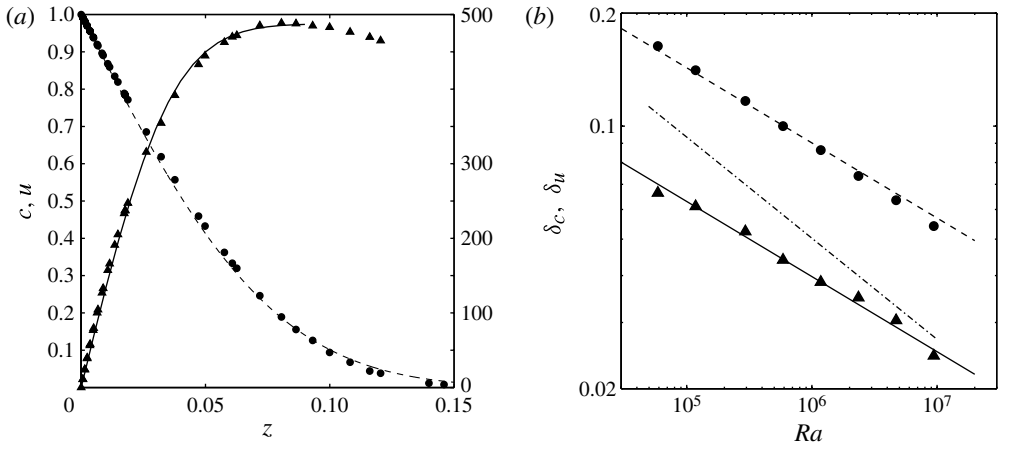


FIGURE 15. (*a*) Numerical profiles of radial velocity (▲) and concentration (●) as a function of z below the surface in the case of no-slip boundary conditions for $Ra = 1.17 \times 10^6$. The solid and dashed lines correspond to the fit by (5.26) and (5.19), respectively. (*b*) Variation of the shear layer thickness δ_u (▲) and the chemical boundary layer thickness δ_c (●) with the Rayleigh number. The solid and dashed lines correspond to fit as $Ra^{-0.2}$. The dash-dotted line corresponds to the concentration thickness δ_c in the free-slip case. Here, $r = 0.5$ and $h = 3$.

Figure 15(*b*) shows that the concentration thickness δ_c is larger than in the no-slip case (plotted as a dotted line). This figure also shows that both thicknesses vary as $Ra^{-0.2}$ so that the ratio δ_u/δ_c can be considered as a constant equal to 0.45. It is surprising to see that this ratio varies by less than 10 % when S varies from 50 to 5000. Since the viscous layer is small, the distribution of concentration $c(r, z)$ is still given by (5.19) as in the slip model, so that the flux is given by (5.20), where Q takes the new form

$$Q' = 2\sqrt{\frac{1}{3} + \sum_{k=0}^{+\infty} \frac{\beta_k}{2k+4}} \int_0^\infty \mathrm{erf}\left[\frac{z'}{\delta_u/\delta_c}\right] [1 - \mathrm{erf}(z')]\, \mathrm{d}z' \simeq 0.1569. \qquad (5.27)$$

Moreover, as noted in § 5.1, the maximum concentration on the axis is equal to 0.7 instead of 1 because the carbon dioxide present in the surface shear layer does not reach the axis. To take this drop into account, the velocity profile can be replaced by a step profile of size $\delta_u/2$ such that the velocity smaller than $0.52u_s$ is set to 0 and the velocity larger than $0.52\,u_s$ is set to u_s. With such a profile, the maximum concentration that is advected by the flow is equal to $1 - \mathrm{erf}(\delta_u/2\delta_c) \approx 0.75$ instead of 1, as observed numerically. As a consequence, the maximum velocity w_0 given by (5.9) and the vertical flux given by (5.12) are 25 % smaller. This can be accounted for by changing $F_l(0)$ into $F_l'(0) = 0.75F_l(0)$ and G_l into $G_l' = 0.75G_l$.

To conclude, the size and amplitude of the plume are given by (5.22) and (5.23) in the no-slip case, where $F_l(0)$, G_l and Q are to be replaced by $F_l'(0)$, G_l' and Q', respectively. These predictions are plotted as dashed lines in figure 14. On the same figure are drawn numerical and experimental results for comparison (round symbols). The scaling exponents remain unchanged, which is in good agreement with the numerical and experimental results. However, this is in contradiction with (Whittaker & Lister 2006*b*), who find that, in the case of a no-slip condition at the

https://doi.org/10.1017/jfm.2012.641 Published online by Cambridge University Press

surface, the velocity amplitude scales as $Ra^{3/5}$. This probably comes from the fact that they consider an infinite geometry where the thickness δ_u is larger than the thickness δ_c. The latter scaling is close to but slightly smaller than the scaling $Ra^{2/3}\,(\ln Ra)^{1/3}$ found in our case.

The surface shear layer correction creates a 30 % drop of the velocity amplitude, in agreement with the 30 % drop observed in the numerics and the experiment. The surface shear layer correction has almost no effect on the size of the plume, as is also observed in the numerical result. Using the approximations of $F_l(0)$ and G_l given in (5.11) and (5.14) allows us to give the scalings for the plume velocity and size

$$w_0 \sim 0.115\, Ra^{2/3}\,(\ln Ra)^{1/3} \quad \text{and} \quad l \sim 1.359\, Ra^{-1/6}\,(\ln Ra)^{-1/3} \tag{5.28}$$

and for the mass Nusselt number

$$Nu \sim 0.670\ (Ra/\ln Ra)^{1/3}\,. \tag{5.29}$$

To summarize, the results provided by the numerical simulations do not argue for a drastic modification of the scaling exponents when considering a no-slip boundary condition at the surface (instead of a free-slip). This is in contradiction with the conclusions of Whittaker & Lister (2006*b*) in the case of a distributed source in a semi-infinite medium for a no-slip boundary condition at the wall ($Nu \sim Ra^{1/5}$), probably due to our confined geometry. All the exponents (or apparent exponents) for l, w_0, δ_c and δ_u related to experimental, numerical and theoretical results are gathered in table 1.

6. Conclusion

In this paper we have presented experimental, numerical and theoretical results on the plume created in water by a pressure step of CO_2. The main difference with previous results in the literature is that the plume is parallel because the Péclet number is larger than the aspect ratio $h = H/R_c$ (which is not the case in experiments with a point source of size $Rc \ll H$). This first experimental and numerical evidence of a finite size plume allows us to confirm the recent analytical result of Whittaker & Lister (2006*b*).

The characteristics of the stationary plume, when it exists, do not depend on the Bond number or the aspect ratio (except for the duration of the stationary stage). The set of experiments reported here covers two decades of Rayleigh number. The maximum velocity w_0, when fitted by a power law, scales as $Ra^{0.72}$ experimentally and numerically (for slip and no-slip boundary conditions at the surface). Theoretical results given by the semi-analytical model presented in the last section are in good agreement since they predict an apparent exponent equal to 0.69 for this range of Rayleigh number. In fact, this apparent exponent comes from the logarithmic correction that appears in the theoretical scaling ($w_0 \sim Ra^{2/3}\,(\ln Ra)^{1/3}$). This scaling law is similar to the one derived by Whittaker & Lister (2006*a*) for a free-slip boundary condition. It should be noted that this scaling still respects the well-known scaling $w_0 \sim \mathscr{R}_f^{1/2}$ (where $\mathscr{R}_f = Ra\,Nu$ is defined using the buoyancy flux), since the Nusselt number scales as $Nu \sim (Ra/\ln Ra)^{1/3}$. The theory properly fits the numerical results for a free-slip condition at the surface and the experimental results for a no-slip boundary condition.

The apparent exponent found for the width l of the plume is equal to -0.23 for experiments, numerics and theory, which can be explained by the theoretical law ($l \sim Ra^{-1/6}\,(\ln Ra)^{-1/3}$), which also contains a logarithmic correction. However,

https://doi.org/10.1017/jfm.2012.641 Published online by Cambridge University Press

theoretical and numerical calculations underestimate the experimental results by about 20–30 % (whatever the Rayleigh number).

In the no-slip case, the viscous layer at the surface is unexpectedly smaller than the diffusive layer, which is surprising given that the kinematic viscosity is greater than the diffusivity of carbon dioxide by about three orders of magnitude. We suppose that this is an intrinsic characteristic of this flow in a confined geometry.

This paper has focused on the stationary stage of the plume. However, the early transient stage, which is governed by the Rayleigh–Taylor instability, also deserves an in-depth study. Since the pressure increases very quickly, this instability can be switched on in a very short time, unlike in classical Rayleigh–Taylor experiments with a heavy fluid located above a lighter one. It would thus be interesting to study the Rayleigh–Taylor instability in this cylindrical geometry, with a time-dependent density. However, the temperature increase due to the compression of the gas modifies the dynamics of the instability. A new set-up has been designed in order to prevent this disturbing effect.

Furthermore, owing to the finite height of the container, the plume gradually fills the bottom with heavy fluid, thus limiting the vertical extension of the plume. When the aspect ratio of the plume is of the order of two, the plume becomes unstable and starts pulsating. This instability has not been described in detail here or in the literature. A thorough study needs to be done in order to understand this phenomenon.

These results are important for geophysical applications, because they give an analytical expression for the Nusselt number and an asymptotic form of the flow within the plume. It thus allows the prediction of the amplitude and fluxes created by convection in the Earth's mantle where the geometry might be confined because of the temperature-dependent viscosity.

Acknowledgements

We would like to thank Y. Tugend and D. Connetable for their help in designing the experimental set-up.

Supplementary movie

Supplementary movie are available at http://dx.doi.org/10.1017/jfm.2012.641.

Appendix A. Calculation of the flow at the surface (free-slip)

We wish to know the flow at the surface induced by the plume on the axis with a velocity profile given by (5.7) for $z \gg l$. The flow inside the cylindrical cavity outside of the plume is the solution of the Navier–Stokes equation for an axisymmetric creeping flow, i.e. taking into account only the viscous term (since the inertial and gravity terms are negligible). Assuming that the velocity derives from the stream function ψ, then

$$u = -\frac{1}{r}\frac{\partial \psi}{\partial z}, \quad w = -\frac{1}{r}\frac{\partial \psi}{\partial r}. \tag{A 1}$$

Following Duda & Vrentas (1971) and Umemura & Busse (1989), the curl of the Navier–Stokes equation leads to the following equation for the stream function outside the plume:

$$D^4\frac{\psi}{r} = 0 \quad \text{with} \quad D^2 = \frac{\partial}{\partial r}\frac{1}{r}\frac{\partial}{\partial r}r + \frac{\partial^2}{\partial z^2}. \tag{A 2}$$

https://doi.org/10.1017/jfm.2012.641 Published online by Cambridge University Press

Assuming a trigonometric dependence on z, we can find three different functions $\sin(kz)f_i(kr)$ that are solutions of this equation for all k with

$$f_0(r) = r^2\mathrm{K}_0(r), \quad f_1(r) = r\mathrm{I}_1(r) \quad \text{and} \quad f_2(r) = r^2\mathrm{I}_0(r), \tag{A 3}$$

where K_i and I_i are modified Bessel functions. The stream function is subject to the boundary conditions $\psi = \partial\psi/\partial r = 0$ at $r = 1$ and $\psi = 0$ at $z = 0, h$ such that the outer streamline follows the container and the surface and such that the vertical velocity is equal to zero at $r = 1$. The stream function can thus be written as a Fourier series:

$$\psi = \sum_{n=1}^{+\infty} A_n \sin\left(\frac{n\pi z}{h}\right)\left[f_0\left(\frac{n\pi r}{h}\right) + \lambda_n f_1\left(\frac{n\pi r}{h}\right) + \mu_n f_2\left(\frac{n\pi r}{h}\right)\right]. \tag{A 4}$$

The coefficients λ_n and μ_n are chosen such that the term in parentheses vanishes and its derivative vanishes at $r = 1$:

$$\lambda_n = \frac{f_0\left(\frac{n\pi}{h}\right) f_2'\left(\frac{n\pi}{h}\right) - f_0'\left(\frac{n\pi}{h}\right) f_2\left(\frac{n\pi}{h}\right)}{f_2\left(\frac{n\pi}{h}\right) f_1'\left(\frac{n\pi}{h}\right) - f_2'\left(\frac{n\pi}{h}\right) f_1\left(\frac{n\pi}{h}\right)}, \tag{A 5}$$

$$\mu_n = \frac{f_0\left(\frac{n\pi}{h}\right) f_1'\left(\frac{n\pi}{h}\right) - f_0'\left(\frac{n\pi}{h}\right) f_1\left(\frac{n\pi}{h}\right)}{f_1\left(\frac{n\pi}{h}\right) f_2'\left(\frac{n\pi}{h}\right) - f_1'\left(\frac{n\pi}{h}\right) f_2\left(\frac{n\pi}{h}\right)}. \tag{A 6}$$

The function $f_0(r)$ is equivalent to $r^2\ln(r)$ when r tends to 0 and is dominant compared to $f_1(r)$ and $f_2(r)$ such that, at leading order, the vertical velocity is equal for small r to

$$w = -2\sum_{n=1}^{+\infty} A_n \frac{n^2\pi^2}{h^2}\ln(r)\sin\left(\frac{n\pi z}{h}\right). \tag{A 7}$$

This solution, valid outside of the plume, must be matched with the solution inside the plume (5.7), which can be approximated when $l \ll r \ll 1$ by

$$w = -\frac{Ra\,l^2}{2}\ln(r), \tag{A 8}$$

because $\int_{r/l}^{1/l}(1 - \mathrm{e}^{-r'^2})\,\mathrm{d}r'/r' \sim -\ln(r)$ for $r \gg l$. Equating (A 7) and (A 8) allows the Fourier coefficient to be calculated as

$$A_n = \frac{h^2}{n^2\pi^2}\frac{Ra\,l^2}{2n\pi}[1 - (-1)^n]. \tag{A 9}$$

As shown by Umemura & Busse (1989), the term corresponding to f_0 in the Fourier series can be calculated explicitly. Indeed, when h tends to $+\infty$, the discrete sum can be transformed into a continuous integral using the polar coordinates ($r = \rho\cos\Phi$, $z = \rho\sin\Phi$), which can then be calculated analytically. The passage from discrete to continuous leads to

$$\begin{aligned}\sum_{n=1}^{+\infty} A_n \sin\left(\frac{n\pi z}{h}\right) f_0\left(\frac{n\pi r}{h}\right) &= \frac{Ra\,l^2}{2\pi}\rho^2\sin^2\Phi\int_0^{+\infty}\mathrm{K}_0(s\sin\Phi)\sin(s\sin\Phi)\frac{\mathrm{d}s}{s} \\ &= -\frac{Ra\,l^2}{4}\rho^2\sin^2\Phi\ln\left(\tan\frac{\Phi}{2}\right).\end{aligned} \tag{A 10}$$

https://doi.org/10.1017/jfm.2012.641 Published online by Cambridge University Press

This term can then be approximated when z tends to 0 (i.e. when Φ tends to $\pi/2$) by $Ra\,l^2 rz/4$. The other terms of the Fourier series can also be approximated when z tends to 0 because $\sin(n\pi z/h)$ is equivalent to $n\pi z/h$. The stream function is thus equal for small z to

$$\psi = \frac{Ra\,l^2 rz}{4}[1 + g_h(r)] \tag{A 11}$$

with

$$g_h(r) = \frac{4h}{\pi^2 r}\sum_{n\ \text{odd}} \frac{\lambda_n}{n^2} f_1\left(\frac{n\pi r}{h}\right) + \frac{\mu_n}{n^2} f_2\left(\frac{n\pi r}{h}\right). \tag{A 12}$$

The function $g_h(r)$ can also be transformed into a continuous integral when h tends to $+\infty$, leading to

$$g_h(r) = \frac{2}{\pi r}\int_0^{+\infty} \left[\frac{f_1(rs)}{s^2}\frac{f_0(s)f_2'(s) - f_0'(s)f_2(s)}{f_2(s)f_1'(s) - f_2'(s)f_1(s)} + \frac{f_2(rs)}{s^2}\frac{f_0(s)f_1'(s) - f_0'(s)f_1(s)}{f_1(s)f_2'(s) - f_1'(s)f_2(s)}\right] \mathrm{d}s. \tag{A 13}$$

Using the power series in r^k of the modified Bessel functions in $f_1(rs)$ and $f_2(rs)$, the integral can be written as a discrete sum:

$$g_h(r) = \sum_{k=0}^{+\infty} \beta_k r^{2k+1} \quad (\text{for } h \to \infty) \tag{A 14}$$

with

$$\beta_k = \frac{2}{\pi k!^2}\int_0^{+\infty} \left(\frac{s}{2}\right)^k \frac{f_0(s)\left[f_1'(s) - \dfrac{1}{2k+2}f_2'(s)\right] - f_0'(s)\left[f_1(s) - \dfrac{1}{2k+2}f_2(s)\right]}{f_1(s)f_2'(s) - f_1'(s)f_2(s)} \mathrm{d}s. \tag{A 15}$$

These coefficients converge rapidly, as shown by the first coefficients: $\beta_0 = -1.4030$, $\beta_1 = 0.3322$, $\beta_2 = 0.0518$, $\beta_3 = 0.0136$, $\beta_4 = 0.0038$, $\beta_5 = 0.0011$ and $\beta_6 = 0.0003$. Introducing this approximate form of g_h into (A 11), dividing by r and differentiating with respect to z gives the analytic form of the radial velocity given by (5.15) in § 5.2.

REFERENCES

ADAMS, E. E., GOLOMB, D., ZHANG, X. Y. & HERZOG, H. J. 1995 Confined release of CO_2 into shallow seawater. In *Direct Ocean Disposal of Carbon Dioxide* (ed. N. Handa & T. Ohsumi), pp. 153–164. Terra Scientific.

ALENDAL, G., DRANGE, H. & HAUGAN, P. M. 1994 Modelling of deep-sea gravity currents using an integrated plume model. In *The Polar Oceans and Their Role in Shaping the Global Environment* (ed. O. M. Johannessen, R.D. Muench & J.E. Overland), pp. 237–246. American Geophysical Union.

ANDERSON, D. 1975 Chemical plumes in the mantle. *Geol. Soc. Am. Bull.* **86**, 1593–1600.

AYA, I., YAMANE, K. & SHIOZAKI, K. 1999 Proposal of self sinking CO_2 sending system: COSMOS. In *Greenhouse Gas Control Technologies* (ed. B. Eliasson, P. W. F. Riemer & A. Wokaun), pp. 269–274. Pergamon.

BATCHELOR, G. K. 1954 Heat convection and buoyancy effects in fluids. *Q. J. R. Meteorol. Soc.* **80**, 339–358.

CAULFIELD, J. A. 1996 Environmental impacts of carbon dioxide ocean disposal: plume predictions and time dependent organism experience. Master's degree report, Massachussets Institute of Technology.

https://doi.org/10.1017/jfm.2012.641 Published online by Cambridge University Press

CONCUS, P. 1968 Static menisci in a vertical right cylinder. *J. Fluid Mech.* **34**, 481–495.

CUSSLER, E. 1997 *Diffusion: Mass Transfer in Fluid Systems*. Cambridge University Press.

DOMBROWSKI, C., LEWELLYN, B., PESCI, A. I., RESTREPO, J. M., KESSLER, J. O. & GOLDSTEIN, R. E. 2005 Coiling, entrainment, and hydrodynamic coupling of decelerated fluid jets. *Phys. Rev. Lett.* **95**, 184501.

DUDA, J. & VRENTAS, J. 1971 Steady flow in the region of closed streamlines in a cylindrical cavity. *J. Fluid Mech.* **45**, 247–260.

FRANK, M. J. W., KUIPERS, J. A. M. & VAN SWAAIJ, W. P. M. 1996 Diffusion coefficients of $CO_2 + H_2O$, $CO_2 + CH_3OH$, $NH_3 + H_2O$, and $NH_3 + CH_3OH$ liquid mixtures. *J. Chem. Eng. Data* **41**, 297–302.

FUJII, T. 1963 Theory of the steady laminar natural convection above a horizontal line heat source and a point heat source. *Intl J. Heat Mass Transfer* **6**, 597.

HEBACH, A., OBERHOF, A. & DAHMEN, N. 2004 Density of water + carbon dioxide at elevated pressures: measurements and correlation. *J. Chem. Eng. Data* **49** (5), 950–953.

LIST, E. J. 1982 Turbulent jets and plumes. *Annu. Rev. Fluid Mech.* **14**, 189–212.

LOMBARDI, M., CAULFIELD, C. P., COSSU, C., PESCI, A. I. & GOLDSTEIN, R. E. 2011 Growth and instability of a laminar plume in a strongly stratified environment. *J. Fluid Mech.* **671**, 184–206.

MEUNIER, P. & LEWEKE, T. 2003 Analysis and optimization of the error caused by high velocity gradients in particle image velocimetry. *Exp. Fluids* **35** (5), 408–421.

MORGAN, W. 1971 Convection plumes in the lower mantle. *Nature* **20**, 42–43.

MORTON, B. R., TAYLOR, G. I. & TURNER, J. S. 1956 Turbulent gravitational convection from maintained and instantaneous sources. *Proc. R. Soc. Lond.* A **234**, 1–23.

MOSES, E., ZOCCHI, G. & LIBCHABER, A. 1993 An experimental study of laminar plumes. *J. Fluid Mech.* **251**, 581–601.

OLSON, P., SCHUBERT, G. & ANDERSON, C. 1993 Structure of axisymmetric mantle plumes. *J. Geophys. Res.* **98**, 6829–6844.

PERA, L. & GEBHART, G. 1971 On the stability of laminar plumes: some numerical solutions and experiments. *Intl J. Heat Mass Transfer* **14**, 975–984.

PESCI, A. I., PORTER, M. A. & GOLDSTEIN, M. A. 2003 Inertially driven buckling and overturning of jets in a Hele-Shaw cell. *Phys. Rev.* E **68**, 056305.

ROBERTS, G. O. 1977 Fast viscous convection. *Geophys. Astrophys. Fluid Dyn.* **8**, 197–233.

SCHLIEN, D. & BOXMAN, R. 1979 Temperature field measurement in an axisymmetric laminar plume. *Phys. Fluids* **22**, 631–634.

SCHOFIELD, S. P. & RESTREPO, J. M. 2010 Stability of planar buoyant jets in stratified fluids. *Phys. Fluids* **22**, 053602.

TURNER, J. S. 1969 Buoyant plumes and thermals. *Annu. Rev. Fluid Mech.* **1**, 29–44.

UMEMURA, A. & BUSSE, F. H. 1989 Axisymmetric convection at large Rayleigh and infinite Prandtl number. *J. Fluid Mech.* **208**, 459–478.

WHITTAKER, R. & LISTER, J. 2006*a* Steady axisymmetric creeping plumes above a planar boundary. Part 1. A point source. *J. Fluid Mech.* **567**, 361–378.

WHITTAKER, R. & LISTER, J. 2006*b* Steady axisymmetric creeping plumes above a planar boundary. Part 2. A distributed source. *J. Fluid Mech.* **567**, 379–397.

WOODS, A. W. 2010 Turbulent plumes in nature. *Annu. Rev. Fluid Mech.* **42**, 391–412.

WORSTER, M. G. 1986 The axisymmetric laminar plume: asymptotic solution for large Prandtl number. *Stud. Appl. Math.* **75**, 139–152.

YBERT, C. 1998 Stabilisation des mousses aqueuses par des protéines. PhD thesis, Université Louis Pasteur (Strasbourg I).

YIH, C. S. 1951 Free convection due to a point source of heat. In *Proceedings of the First U.S. National Congress of Applied Mechanics*, pp. 941–947.

https://doi.org/10.1017/jfm.2012.641 Published online by Cambridge University Press